LETTERS IN BIOMATHEMATICS
An International Journal

RESEARCH ARTICLE

OPEN ACCESS

Biomathematical Analysis of Nanoparticle-Based Biomaterials for Targeted Drug Delivery Applications

Hammad Tayyab[1*], Umair Rauf[2], Muhammad Asad Asghar[3]

[1*]Interdisciplinary Research Center in Biomedical Materials (IRCBM), COMSATS University Islamabad, Lahore Campus, Pakistan; [2]Department of Chemistry, Quaid-i-Azam University Islamabad; [3]Department of Chemistry, School of Natural Sciences, National University of Sciences and Technology Islamabad Pakistan

ABSTRACT

This study expresses the biomathematical analysis of biomaterials which are nanoparticles based for the drug delivery. As, in vivo behavior of the nanoparticles for the drug delivery is complex and unpredictable. In particular, among different types of nanoparticles that introduce dimensionless groups carrying permeability and phagocytic uptake. This shifts the model from merely descriptive simulation to a predictive and theory-driven biomathematical framework by offering a generalized mathematical interpretation of biodistribution behavior. So, a physiologically based pharmacokinetic (PBPK) model was developed in rats and it was employed to check out the behavior and distribution of in vivo in the four different nanoparticles (PEG-PAA, PAA, TiO_2 and gold). This study introduces dimensionless framework based on phagocytosis and permeability numbers which are key factors for the distribution nanoparticles-based biomaterials. Moreover, the model provides predictive information beyond traditional PBPK parameter fitting by clarifying how rising phagocytic activity generates quick and improved organ accumulation. The model allows for precise modeling of nanoparticle movement and accumulation throughout organs by taking into consideration tissue-specific blood flow, permeability, and saturable uptake by phagocytic cells. The important factors of biokinetic behavior also indicate phagocytic, organ specific permeability and physiochemical properties of nanoparticles. This study is the key finding in the extension of PBPK modeling for optimization of designing nanoparticle and improving targeted drug delivery and acts as a productive tool.

ARTICLE HISTORY
Received February 15, 2026
Accepted Apri 27, 2026

KEYWORDS
Biomathematical,
Biomaterials,
Nanoparticles,
Physiologically Based Pharmacokinetics (PBPK),
Drug Delivery

1. Introduction

A quantitative foundation for comprehending and forecasting the intricate relationships between NPs and biological systems is provided by biomathematical analysis (Fjóla, 2025). Biomathematical modeling makes it possible to systematically assess NP transport, distribution, and elimination mechanisms by combining concepts from applied mathematics, biomechanics and systems biology. Specifically, PBPK models are an effective biomathematical tool that predicts drug distribution by combining compound-specific pharmacokinetic characteristics with species-specific anatomical and physiological data (Ozbek et al., 2024). The structural and functional matrices that control therapeutic efficacy are provided by biomaterials, which constitute the basis of NP-based drug delivery systems (Wang et al., 2025).

Understanding the connections between material features (composition, surface chemistry, biodegradability) and biokinetic results is necessary for the logical design of biomaterial-based NPs. PEGylated polyacrylamide (PEG-PAA) and other polymeric biomaterials provide adjustable surface characteristics that decrease interaction and increase circulation time (Onofri et al., 2025). Titanium dioxide and gold are two examples of metallic biomaterials with unique physicochemical characteristics suitable for imaging and scientific applications (Wu et al., 2025). Current study aimed to expand a model for the PBPK of NPs such as PEGylated polyacrylamide (PAA-PEG) NPs that was previously published (Li et al., 2014). The biodistribution of PAA-PEG NPs in rats after a single intravenous injection serves as the basis for the model created by Li et al. (2014); Wenger et al. (2011). Here, it is also provided information about intravenous administration of gold, titanium dioxide (TiO_2), and uncoated polyacrylamide (PAA) NPs to rats (Shinohara et al., 2014; Wang et al., 2010; Wenger et al., 2011).

This paper suggests a dimensionless biomathematical framework based on phagocytosis number (Ø) and permeability

CONTACT Hammad Tayyab: hammad.tayyab.pk@gmail.com

number (Ψ) to describe nanoparticle transport dynamics, in contrast to the existing nanoparticle PBPK models that are mostly experimentally fitted. This resolves the structural overparameterization issue that is present in NP-PBPK models and has been found to be a significant obstacle to the models' generalizability. In this work, we combine dynamical systems theory, dimensionless analysis, and data-driven parameter reduction to create a generalizable biomathematical framework for comprehending and forecasting the biodistribution of nanoparticle-based biomaterials, transitioning from case-specific modeling to a unified theoretical description. Up until now, no one has really attempted to use dimensionless scaling with NP-PBPK systems. This effort seems to be the first to achieve it.

2. Objective of Research Study

This paper aims to build an enlarged biomathematical theory of nanoparticle biodistribution using physiological-based pharmacokinetics (PBPK). By lowering parameters and adding dimensionless values like phagocytosis number (Ø) and permeability number (Ψ), the mathematical model is intended to be made simpler. Moreover, the model aims to classify nanoparticle behavior into different transport regimes according to underlying physiological systems. The ultimate goal is to provide a modeling framework for drug delivery systems enabled by nanoparticles-based biomaterials that is both scalable and comprehensible.

3. Literature Review

Studies show that a physiologically based pharmacokinetics (PBPK) modeling is a useful pharmacological approach to guide the design of nanoformulations and hence optimize their PK. This modeling method has been effectively applied to both simulations of pertinent clinical scenarios and conventional formulations in drug development programs (Karlsson et al., 2013). Both physiological (such as tissue volume, tissue blood flow, and the quantity of metabolizing enzymes and transporters) and drug-specific (such as clearance and tissue partition coefficient k_p) parameters are used to parameterize PBPK models. Together, these parameters define drug disposition within the physiological system (Jones & Rowland-Yeo, 2013). Simplified perfusion-limited or permeability-limited frameworks were used in early NP-PBPK models. NP-specific processes, such as protein corona formation and saturable clearance by the mononuclear phagocyte system, have been included in more recent research (Yuan et al., 2019). Instead of concentrating on basic mathematical issues, the study has mostly concentrated on phenomenological parameter fitting (Cho et al., 2024). With 9 – 15 NP-specific parameters, NP-PBPK models are complicated, leading to unidentifiable parameter estimations and impractical forecasts for novel NP types (Dadashova et al., 2024).

Although parameter subset selection in other PBPK settings has been addressed in recent work, there is currently no systematic method for parameter reduction in NP-PBPK models (Carlander et al., 2016). Second is the sensitivity analysis, significance of interacting factors and non-linear effects is consistently underestimated by standard one-at-a-time (OAT) approaches that change parameters one at a time by ± 10%. From the standpoint of biomaterials, mathematical modeling has been crucial in figuring out how material characteristics affect NP behavior. Permeability and phagocytic uptake are significantly changed by factors such NP size (31 nm for PAA vs. 13×56 nm for gold nanorods) and surface coating (PEG vs. CTAB vs. untreated) (Brown et al., 1997; Jain et al., 2015). Studies also explain that a logical foundation for optimizing NP design is provided by this biomaterial-modeling integrated method, which permits systematic analysis of how design decisions in biomaterial synthesis translate to quantifiable variations in biodistribution. The current models are "one-off" constructs that are calibrated to a particular NP type and dose, they lack a mathematical framework that enables prediction of unproven NP behavior without total parameterization. The literature has examined dimensionless analysis and parameter reduction as solutions to this problem. For instance, Le et al. (2022) exhibited a simpler model building with sensitivity-driven parameter reduction, whereas Carlander et al. (2016) offered generalized PBPK models for nanoparticles-based biomaterials. An essential requirement that this work fills are the systematic application of dimensionless scaling to unify the transport behavior of nanoparticles, which has not been thoroughly investigated (Bernareggi & Rowland, 1991; Eriksson et al., 2004).

4. Methods

4.1 Collection of Experimental Data

Experimental data from the literature about the biodistribution of NPs given intravenously to rats in a single dosage. In order to quantify the amounts in urine, feces, and ten distinct tissues and organs, Wenger et al. (2011) used some nanoparticles-based biomaterials like PAA nanospheres that were either uncoated (PAA) or coated with polyethylene glycol (PAA-PEG) and both tagged in the polymer chain with [^{14}C]. Dynamic light scattering revealed that the uncoated PAA had a diameter of 31 nm and a log-normal distribution; however, the charge was not disclosed. Three to twelve sampling time

points were employed, and the dosages for PAA-PEG and PAA were 7 and 11 mgEq/rat, respectively. Shinohara et al. (2014) studied TiO_2 nanospheres with an average size of 63 nm (determined by dynamic light scattering) and a Z-potential of −43 mV in aqueous disodium phosphate solution, however, coating is not mentioned. After injection at a concentration of 0.95 mg particles per kg body weight, inductively coupled plasma with a sector field mass spectroscopy was employed to monitor the amount of TiO_2 NPs in eight different tissues and organs at five different sampling times. Using transmission electron microscopy, Wang et al. (2010) examined gold nanorods capped with cetyltrimethylammonium bromide (CTAB) that had a Z-potential of 29 mV in saline and measured 13 nm in diameter and 56 nm in length. These various NPs' traits are summed up in (Table 1).

Table 1: An Overview of the Four Research that Form the Basis of Physiologically Based Pharmacokinetic Model (Carlander et al., 2016)

Material	PAA	PAA	Gold	TiO_2
Coating	PEG	No	CTAB	No
Shape	Sphere	Sphere	Rod	Sphere
Dose (μg)	7000	11000	90	232
Size (Nm)	D: 31	D: 31	L: 56, D: 31	D: 13
Size Determined by	DLS	DLS	TEM	DLS
Sampling Times (Hours)	0.08, 0.17, 0.5, 1, 4, 8, 24, 48, 72, 96, 120	0.08, 0.17, 0.33, 0.67, 1, 2, 4, 8, 24, 72, 96, 120	0.5, 1, 4, 16, 24, 72, 168, 336, 672	6, 24, 72, 168, 720
Rat Strain	Crl CD®(SD)IGS BR	Crl CD®(SD)IGS BR	Sprague Dawley	F344/DuCrlCrlj
Mean Body Weight (g	253.4	253.4	160	244
Organs Monitored	Bl, Li, Sp, Lu, Ki, He, Br, Lymp, BM, carcass	Bl, Li, Sp, Lu, Ki, He, Br, Lymp, BM, carcass	Bl, Li, Sp, Lu, Ki, He, Br, Bo, Mu	Bl, Li, Sp, Lu, Ki, He, Br. Lymp
Excretion	U + F	U + F	U + F	U + F
Analytical Method	Cl4	Cl4	ICP-MS	ICP-SFMS
Reference	Wenger et al. (2011)	Wenger et al. (2011)	Wang et al. (2010)	Shinohara et al. (2014)

Abbreviations: PAA, Polyacrylamide; PEG, Polyethylene Glycol; CTAB, Cetyltrimethylammonium Bromide; TiO_2, Titanium Dioxide; Bl, Blood; Li, Liver; Sp, Spleen; Lu, Lung; Ki, Kidney; He, Heart; Br, Brain; Lymp, Lymph Nodes; BM, Bone Marrow; Bo, Bone; Mu, Muscle; U, Urine; F, Feces; DLS, Dynamic Light Scattering; TEM, Transmission Electron Microscopy; ICP, Inductively Coupled Plasma; MS, Mass Spectrometry; And SFMS, Sector Field Mass Spectrometry.

4.2 Calculation of Tissue Content

Before fitting the model, the background levels of TiO_2 in unexposed animals were deducted from the values found in exposed animals. A value equal to half of the detection limit was given to observations that fell below it. When required, distributions were converted to mass per organ using reference values from the literature or, if available, dosage and biometric data from the research (Brown et al., 1997; Eriksson et al., 2004).

4.3 Genetic Algorithm (GA) Based Grouping to Reduce Parameter Space

A model was developed to commonly discuss basic parameters which are used for PBPK models in nanomaterials, in this, a novel GA based approach is implemented to resolve problem of unattainable and structurally unclear estimation of parameters (Cho et al., 2024).

$$F(g) = AIC(g) + \lambda.|g| \quad (1)$$

where λ is a penalty coefficient (λ = 2 selected by cross-validation), AIC(g) is the Akaike Information Criterion of the model with grouping g, and |g| is the number of different groups.

4.4 PBPK Mathematical Formulation

4.4.1 Representation of Dimension

Non-linear dimension which are developed from principles of mass balance for the biodistribution of nanoparticle-based biomaterials among physiological compartments.

$$M(t) = M_1(t), M_2(t) \ldots . M_n(t) \quad (2)$$

It indicates the nanoparticles masses in every compartment, and then organ is divided into subcompartments i.e.

blood (B), tissue (T) and phagocytosis (PC). The equation is governed by:

$$\frac{dM}{dt} = F\ (M, \theta) \tag{3}$$

where θ is a vector of model parameters, such as blood flow rates, permeability coefficients, and phagocytic uptake rates, and F is a nonlinear vector-valued function that represents physiological transport.

4.4.2 Equations of Mass Balance Compartments

The model comprises ten tissue compartments (blood, liver, spleen, lung, kidney, heart, brain, bone marrow, lymph nodes, and carcass) and each compartment is subdivided into three subcompartments (blood (B), tissue (T), and phagocytic cells (PC)).

Blood Subcompartments:

$$\frac{dM_{B,i}}{dt} = Q_i\ (C_{B,art} - \frac{M_{B,i}}{V_{B,i}} - P_i S_i\ (\frac{M_{B,i}}{V_{B,i}} - \frac{M_{T,i}}{V_{T,i}}) \tag{4}$$

Tissue Subcompartments:

$$\frac{dM_{T,i}}{dt} = P_i S_i\ \left(\frac{M_{B,i}}{V_{B,i}} - \frac{M_{T,i}}{V_{T,i}}\right) - K_{ab,i} \cdot \frac{M_{T,i}}{V_{T,i}} \cdot \left(1 - \frac{M_{PC,i}}{M_{PC,i}^{sat}}\right) \tag{5}$$

Phagocytosis Subcompartments:

$$\frac{dM_{PC,i}}{dt} = K_{ab,i} \cdot \frac{M_{T,i}}{V_{T,i}} \cdot (1 - \frac{M_{PC,i}}{M_{PC,i}^{sat}}) \tag{6}$$

The specific model to introduce the non-linear kinetics that represent the phagocytosis uptake.

$$1 - \frac{M_{PC,i}}{M_{cap,i}} \tag{7}$$

here, M_B, M_T, M_{PC} are the masses of the subcompartments (blood, tissue and phagocytosis), V_B, V_T are the volumes, Q_i is the blood flow rate. P_i is permeability co-efficient; S_i is change in surface area.

4.4.3 Dimensionless Analysis

For each compartment organ *i*, examining the dimensionless groups reveals that the way nanoparticles disperse throughout the body depends on which processes perfusion, permeability, or phagocytic saturation take the lead. What matters most is the balance of the parameters, not the precise quantities. Here, M indicates the scale of mass, and T indicates time scale,

$$M = \frac{M}{M_{cap}}, T = \frac{t}{t_c} \tag{8}$$

The equation of the tissues yields,

$$\frac{dM_t}{dt} = \Psi(M_B - M_T) - \emptyset M_T(1 - \frac{M_{PC}}{M_{cap}}) \tag{9}$$

Phagocytosis Number:

$$\emptyset = \frac{k_{ab} M_{cap}}{Q} \tag{10}$$

Permeability Number:

$$\Psi = \frac{PS}{Q} \tag{11}$$

The ratio of phagocytic uptake capacity to convective transport is represented by the parameter Φ, while the relative relevance of permeability vs blood flow is measured by the value Ψ. The model moves from descriptive simulation to theory-driven prediction thanks to these dimensionless groups, which allow for a unifying mathematical framework regardless of particular NP type.

The numbers of these dimensions define transport regime:

- $\emptyset > 1$: It indicates that phagocytosis is dominated
- $\emptyset < 1$: It tells that there is a limited transport of blood flow
- $\Psi > 1$: Equilibrium is maintained rapidly between blood and tissue
- $\Psi < 1$: It restricts the tissue penetration

4.4.4 Parameter Grouping

Two differential equations, one for the tissue and one for the capillary blood, characterize the change in TiO_2 mass in each organ. Below is the general form of the ODEs for each organ's tissue and capillary blood components:

$$\frac{dM_{capi}}{dt} = Qi\left(C_{art} - C_{capi}\right) - x_i Q_i \left(C_{capi} - \frac{C_i}{P_i}\right) \quad (12)$$

$$\frac{dM_i}{dt} = x_i Q_i \left(C_{capi} - \frac{C_i}{P_i}\right) \quad (13)$$

In this equation, the concentrations (C_{capi}, C_i) of TiO_2 NPs in the capillary blood and tissue space of organ i (in μg TiO_2/g tissue), the $(M_{capi}\ and\ M_i)$ mass of TiO_2 NPs (in μg), the blood flow that penetrates organ i (in ml/h), the C_{art} concentration of TiO_2 NPs in arterial blood (in μg TiO_2/g blood), and the permeability coefficient (unitless) express the TiO_2 transportation rate constant with direction.

4.5 PBPK Model

The PBPK model created by Li et al. (2014) was modified and used. To put it briefly, this model consists of 10 compartments, each of which has subcompartments for PCs, tissue, and blood (Figure 1). The physiological parameters (Table 2) were identical to those employed by Li et al. (2014). The model was modified and the following assumptions were made.

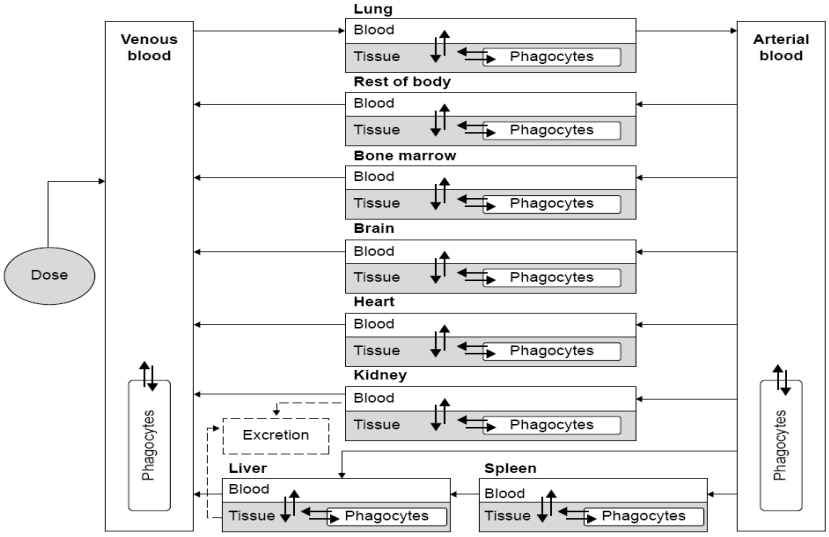


Figure 1: Diagrammatic Representation of Pharmacokinetic Model Based on Physiology (Li et al., 2014)

Notes: Blood, Tissue, and Phagocytic Cells are Represented by the Three Subcompartments that Make up Each of the 10 Compartments. Physiologically Based Pharmacokinetic Modeling of Polyethylene Glycol-Coated Polyacrylamide Nanoparticles in Rats.

Table 2: Parameters in a Physiologically Based Pharmacokinetic Model that are Independent of Nanoparticles

Parameters	Tissues and Organs								
	Blood	Liver	Spleen	Lung	Kidney	Heart	Brain	Bone Marrow	Carcass
Fraction of Total Cardiac Output to Tissue[a]	--	0.183	0.0146	1	0.14	0.051	0.02	0.0267	0.564
Fraction of Total Body Weight[a]	0.074	0.034	0.002	0.005	0.007	0.003	0.006	0.03	0.893
Fraction of Blood in Different Tissue[a]	0.2 Arteries 0.8 Venous	0.21	0.22	0.36	0.16	0.26	0.03	0.1	0.04
Fraction of Residual Blood in Brain[b]	--	--	--	--	--	--	0.346	--	--
Fraction of Residual Blood in Tissue[b]	--	0.177	0.177	0.177	0.177	0.177	--	0.177	0.177

Notes: [a]Literature Values (Bernareggi & Rowland, 1991; Brown et al., 1997; Travlos, 2006). [b]As estimated by Li et al. (2014).

In contrast to Li's model, this tissue was given a low permeability (coefficient of permeability from blood to brain [X_{brain}]) because it has been demonstrated that gold and TiO_2 NPs are absorbed into the brain (Frigell et al., 2014; Geraets et al., 2014; Kolhar et al., 2013; Sonavane et al., 2008; Yokel et al., 2013). Three sets of blood-organ permeability coefficients were examined. The first set used the same grouping as the Li model: all organs save the brain were given a high coefficient of permeability (X_{fast}), while the carcass (X_{rest}) was thought to have a medium permeability (Li et al., 2014). In the second group, bone marrow, heart, lung, and kidney were given X_{rest}, while the liver and spleen were given X_{fast}. The PCs in the liver and spleen have far more direct interaction with blood than those in other compartments, which is the basis for these assignments (Saba, 1970; Sarin, 2010). In the third batch, X_{fast} was applied to the liver, spleen, and bone marrow, which has phagocytic-capable sinusoidal reticuloendothelial blood capillaries that provide easier access to NPs in blood (Sarin, 2010).

In the Li model, the maximum phagocytic capacity per gram tissue ($M_{tissuecap}$) was calculated by multiplying the number of PCs per gram tissue (N_{tissue}, NP-independent, tissue-dependent) by the capacity per PC (maximal uptake capacity per phagocytic cell M_{capi}), a value that is NP-specific and tissue-independent) (Li et al., 2014). This produced one extra parameter (M_{capi}) for each of the four types of NP. Equation 1 was used to determine the initial value of $M_{capPAA\text{-}PEG}$ (before to reoptimization) using the absorption capacity in liver ($M_{livercap}$) published by Li et al. and the number of PCs per gram liver (N_{liver}) described by Alpini et al. (1994).

$$M_{capPAA-PEG} = \frac{M_{livercap}}{N_{livercap}} \tag{14}$$

Li's ($M_{tissuecap}$) values were divided by this using $M_{capPAA\text{-}PEG}$ to determine the initial N_{tissue} values for the remaining tissues (Equation 2):

$$N_{tissue} = \frac{M_{tissuecap}}{N_{capPAA-PEG}} \tag{15}$$

The rat numbers supplied by Brown et al. (1997) were normalized to the mean body weights of the animals used in the various investigations in order to determine the physiological parameters (organ weights, proportion of blood in organs, and fractional blood flow to organs) for the PBPK model.

4.6 Properties of Model

The model was prepared to steady state and identified the system of delivery drug in the subcompartments. A systematic approach was developed to stable the state of drug delivery. To set the ordinary differential equations (ODEs) to zero from the tissue, there are some systematic equations were developed:

From blood:

$$M_{B,i}^{SS} = \frac{Q_i V_{B,i} C_{B,art}^{SS} + {P_i S_i V_{B,i} M_{T,i}^{SS}}/{V_{T,i}}}{Q_i + P_i S_i} \tag{16}$$

From tissue:

$$M_{T,i}^{SS} = \frac{{P_i S_i V_{T,i} M_{B,i}^{SS}}/{V_{B,i}}}{P_i S_i + K_{up,i}(1 - M_{PC,i}^{SS}/M_{PC,i}^{sat})} \tag{17}$$

Phagocytic compartment can reach to the saturation when $M_{PC,i}^{SS} = M_{PC,i}^{sat}$. In this way, this saturation elaborates carrying ability of the sub compartment.

4.7 Optimization of the Model

To find feasible beginning conditions, optimization was carried out for PAA, gold, and TiO_2 NPs by visual comparison with the experimental results before formal calculation of the parameters. The original settings for PAA-PEG were the parameters described by Li et al. Then, using the same number of PCs in each tissue, N_{tissue}, for each of the four NPs, the model was run concurrently with the data sets. The clearance to feces (rate of clearance in feces [CL_f]) and urine (rate of clearance in urine [CL_u]), the rates of PC uptake in the spleen (rate constant for uptake by PCs in the spleen [k_{sab0}]) and other organs (rate constant for uptake by PCs [k_{ab0}]), the blood: tissue partition coefficient (P), the maximal uptake per PC (M_{capi}), and the three coefficients for permeability between blood and tissues (X_{fast}, X_{rest}, and X_{brain}).

4.8 Sensitivity Analysis

To determine how each parameter would impact NP exposure in the liver and spleen, a local sensitivity analysis was

conducted. Each parameter was changed separately for the analysis by ± 10% of the starting value, and the percentage changes in the area-under-the-curve (AUC) outputs for the liver and spleen were reported (Aborig et al., 2019). It was also examined local analytical sensitivity in addition to computational sensitivity analysis.

$$S_i = \frac{\partial \log(AUC)}{\partial \log(\theta_i)} \tag{18}$$

Saturation terms are primarily responsible for nonlinear sensitivity, which indicates that even a slight change in a parameter can have a significant effect when ∅ is large. This explains the significant nonlinear behavior of gold and TiO_2 nanoparticles.

Table 3: Parameters for GSA in PBPK Models

NP Type	Parameter	μ (mean)	σ (Standard Deviation)	S_{Ti}	Classification
PAA-PEG	k_{ab0}	1.25	1.08	0.65	Non-Linear
	CL_f	0.91	0.84	0.52	Non-Linear
	X_{fast}	0.78	0.41	0.48	Linear
PAA	k_{ab0}	1.44	1.22	0.71	Non-Linear
Gold	M_{cap}	2.17	1.89	0.88	Non-Linear
	X_{brain}	1.98	1.67	0.82	Non-Linear
	Dose	1.79	0.35	0.55	Linear
TiO_2	k_{ab0}	6.54	5.98	0.91	Non-Linear

Notes: Global Sensitivity Analysis Parameters (Hsieh et al., 2018; Le et al., 2022)

4.9 Goodness of Fit

By visually comparing the experimental and projected time-courses for the levels of NP in the various tissues, the goodness of fit was maximized (Figure 2). The quality of fit for all experimental and projected data points was then determined (Table 4) by comparing log likelihood values (acslX Libero™), R^2 values (linear regression analyses of log values), and PBPK indices (using log values).

Table 4: The Goodness of Fit

Serial No.	Organs with X_{fast}	Organs with X_{rest}	Log Likelihood[b]	R^{2c}	PBPK Index[d]
1	Li, Sp, BM, Lu, Ki, He	Carcass	-1530	0.955	0.347
2	Li, Sp	Carcass, Lu, Ki, He, BM	-1510	0.956	0.344
3	Li, Sp, BM	Carcass, Lu, Ki, He,	-1507	0.968	0.219

Notes: The Quality of Fit is Compared Using Several High and Medium Blood-Tissue Permeability Assignments. The Computations Took into Account all Four Kinds of Nps. As in Li et al. (2014). The Acslx Libero[tm] Program was Used to Generate Overall Log Likelihood Values, a Greater Value Denotes a Better Match. After Log Transformation, Overall R^2 Values are Computed. As Recommended by Krishnan et al. (1995).

5. Results

The modified model of PBPK was applied to all the three sets of blood-organ coefficients of permeability for the finding of potential differences in the profile of biokinetic profiles of PAA-PEG, PAA, god and TiO_2 NPs. The third, or the one with a high coefficient of permeability (X_{fast}) for the liver, spleen, and bone marrow, was chosen for usage based on the quality of fit (the greatest R^2, lowest log-likelihood value, and lowest PBPK index value (as shown in Table 4).

Despite the four varieties of NP having very diverse physicochemical characteristics and biokinetic profiles, the model was able to represent their biokinetic behavior by adjusting the NP-specific parameters. With slopes and intercepts near unity and zero, respectively, linear regression analysis showed strong correlations between the expected and observed amounts (log10 values) in different tissues in all four cases (R^2 for PAA-PEG was 0.96, for PAA 0.94, for gold 0.88, and for TiO_2 0.91).

5.1 Parameter Grouping to Reduce Dimensions

The TiO_2 PBK model's prediction ability was evaluated using goodness-of-fit data from three separate in vivo experiments that were not engaged in parameter calibration (Geraets et al., 2014). Interestingly, in order to match the model's output units, the reported tissue concentrations had to be converted from titanium (Ti) concentrations to TiO_2 content. The observed concentrations were multiplied by the molecular weight of TiO_2 and then divided by the molecular

weight of Ti to get this conversion.

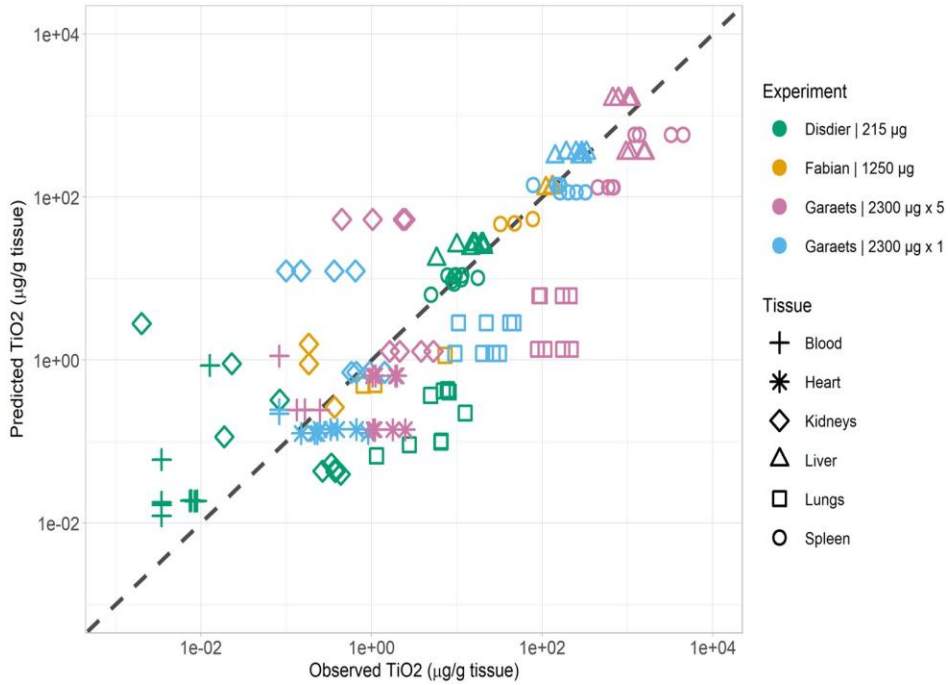


Figure 2: Predictions of the Model Generated Using the Free Parameter Grouping Scheme

5.2 Biokinetics of Specific Nanoparticles

These biokinetic variations between NPs may be mathematically explained by their dimensionless numbers. The system functions in a domain where permeability and phagocytosis are roughly balanced against perfusion for PAA-PEG NPs. Enhanced phagocytic absorption of PAA NPs causes the system to move toward phagocytosis-dominated clearance. The nearly immediate organ accumulation for gold nanorods can be explained by the system being in a domain where both processes are fast in relation to perfusion. Since the system is permeability-limited for TiO_2 NPs, any increases in phagocytic uptake should have little impact on net organ accumulation.

5.2.1 PAA-PEG NPs

All organs showed high agreement between the simulated and actual levels of PAA-PEG NPs, with the exception of bone marrow, where the moderate fit likely reflected the wide variation in the observed data. Moreover, parameter values (with a few exceptions) and the morphologies of the fitted time-courses were nearly comparable to those of Li et al. (2014) indicating that there are some little changes have little effect on the predicted behavior of PAA-PEG NPs.

5.2.2 NPs of Uncoated PAA

With the exception of urine and bone marrow, all compartments showed good or fair concordance between the simulated and actual biodistribution of uncoated PAA NPs. According to the sensitivity analysis, changes in the model parameters had little effect on the time-courses for the majority of tissues. The dosage, body weight, and blood weight were the only variables that influenced fecal excretion at 10 hours only (defined as showing a normalized SA below 1.5 or above 1.5).

5.2.3 Gold Nanorods

An overall R2 value of 0.878 indicates that the biokinetic profiles of the gold nanorods (Figure 3 iii) exhibited acceptable agreement with values published by Wang et al. for most organs, but they differed significantly from those of PAA and PAA-PEG. The levels in the various compartments were impacted by a number of factors, particularly near the conclusion of the 672 hours of observation, according to the sensitivity analysis. The dosage (normalized SAs of 1.5 – 4.5 for many compartments) was the most important factor.

5.2.4 Titanium Oxide

Overall, there was a considerable degree of consistency between the simulated and observed time-courses for the

accumulation of TiO_2 in the different organs. However, similar to the gold nanorods, the model was unable to explain the gradual long-term decline in organs like the kidney and lung that have comparatively low levels of TiO_2. No significant sensitivity was found in the sensitivity analysis, with no normalized SAs below −1.5 or above +1.5.

The PCs in the majority of organs were far from saturated with TiO_2 NPs due to the modest dosage given (Figure 3 iv). Moreover, the biokinetic profile was comparable to that of gold nanorods, with the most noticeable accumulation occurring in the liver and bone marrow, and PCs quickly absorbed 100% of the injected dose and held onto it for the duration of the observation period (Figure 3 iv).

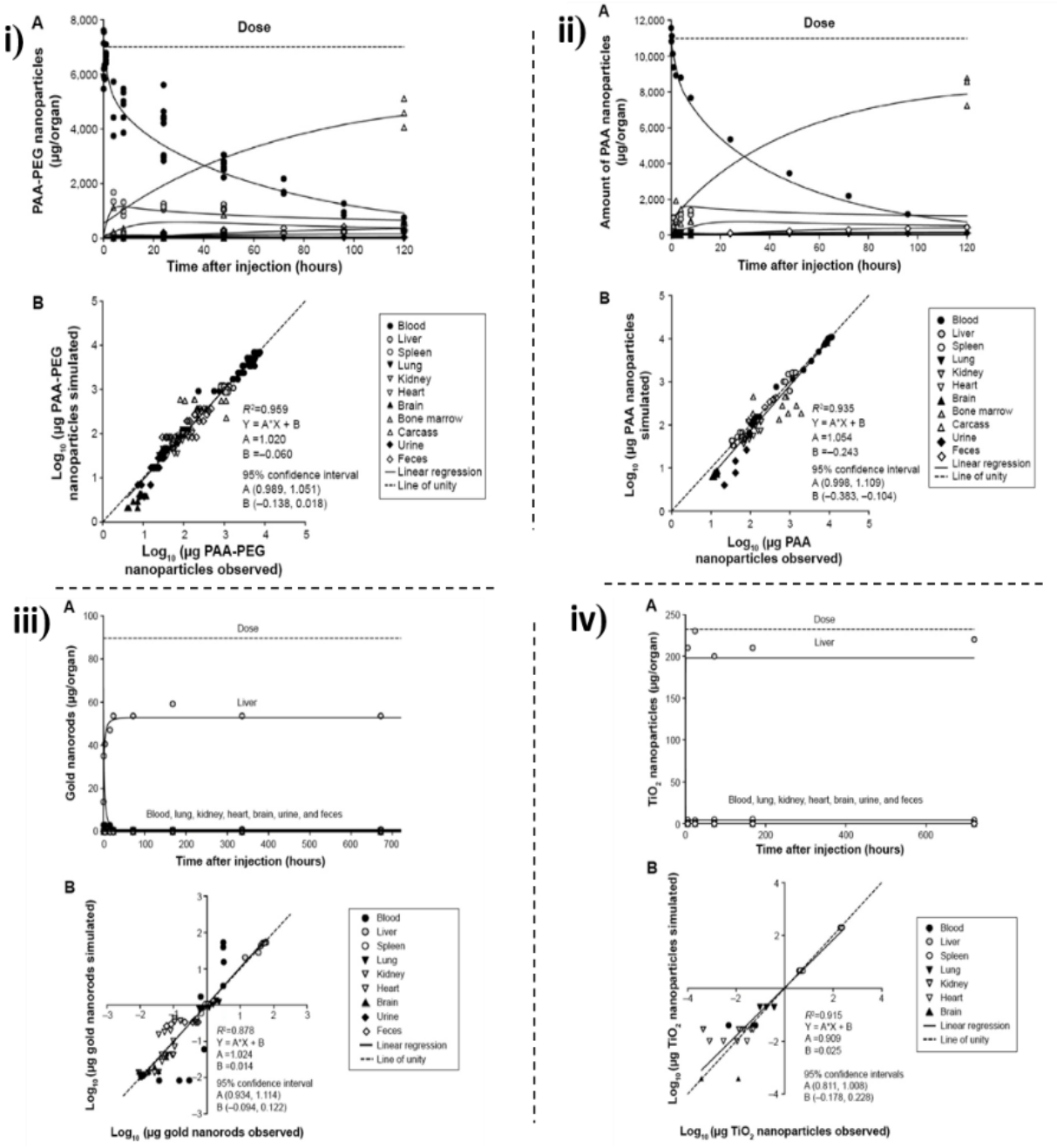


Figure 3: The Biokinetics of PEGylated Polyacrylamide (PAA-PEG), Polyacrylamide (PAA), Gold and Titanium Oxide (TiO_2) Nanoparticles

In the figure 3 (i), the quantity of PAA-PEG nanoparticles in various rat tissues and organs at different time periods after a single intravenous injection of 7,000 µg was both simulated and experimentally measured. The experimental data are from Wenger et al. (2011). (A) Time-courses that were observed (symbols) and simulated (solid lines). (B) For each

data point included in the study, the logs of the simulated and actual values are compared. In the figure 3 (ii), the concentrations of PAA nanoparticles in various rat tissues and organs at different time periods after a single intravenous injection of 11,000 µg were both simulated and experimentally measured (Wenger et al., 2011). (A) Simulated (solid lines) and observed (symbols) time-courses comprise the experimental data. (B) For each data point included in the study, the logs of the simulated and actual values are compared. In the figure 3 (iii), the concentrations of gold nanorods in various rat tissues and organs after a single intravenous injection of 89.6 µg were both experimentally measured and simulated at different time periods (Wang et al., 2010). (A) Simulated (solid lines) and observed (symbols) time-courses comprise the experimental data. (B) For each data point included in the study, the logs of the simulated and actual values are compared. In the figure 3 (iv), the concentrations of TiO_2 nanoparticles in various rat tissues and organs at different time periods after a single intravenous injection of 232 µg were both simulated and experimentally measured (Shinohara et al., 2014). (A) Simulated (solid lines) and observed (symbols) time-courses comprise the experimental data. (B) For each data point included in the study, the logs of the simulated and actual values are compared. At every time point, the urine and feces readings were 0 (not displayed).

5.3 Sensitivity Analysis

Key parameters were disrupted by ± 10% in order to evaluate the relative significance of each step in the biodistribution of NPs following IV injection in mice. The ensuing changes in liver and spleen AUC outputs are presented in Figure. In contrast to spleen exposure, which is more sensitive to changes in cellular absorption, liver exposure is more susceptible to changes in extravasation (such as solute radius).

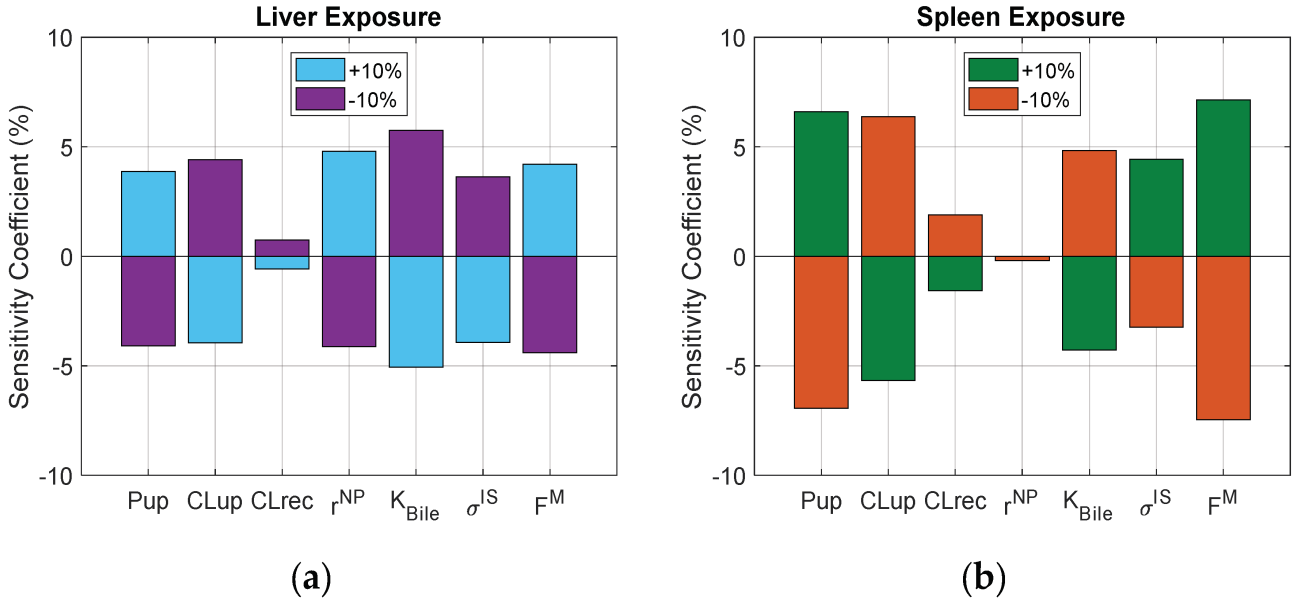


Figure 4: Sensitivity of Liver (a) and Spleen (b) Exposures to Relative Perturbations in Key Parameters

The model results show that certain transport mechanisms controlled by nonlinear system dynamics predominate from a biomathematical standpoint. The sensitivity indices and system responses show the substantial nonlinearities introduced by the interaction between phagocytic uptake and permeability-limited transport. Specifically, rather than being strictly factual findings, the observed differences in nanoparticle accumulation among organs can be understood as emergent features of the underlying dynamical system. This demonstrates how the model's mathematical structure can describe mechanistic activity.

5.4 ∅ – Ψ Regime

In the figure 5, there is a positioning of different nanoparticle with the help of ∅ – Ψ regime in which there is a transport of distinct behaviors by physiochemical properties. PAA-PEG are found in close proximity to the transition area (∅ = 1, Ψ = 1), describing a balance between circulation and cellular absorption. At high rates of cellular absorption, uncoated PAA nanoparticles enter a regime dominated by phagocytosis. The high ∅ and Ψ area, which is linked to rapid equilibration and high organ accumulation, contains gold nanorods. However, TiO_2 nanoparticles are in the permeability-limited regime (Ψ), where biodistribution is controlled by restricted tissue penetration. This categorization provides a

prediction framework that goes beyond case-by-case parameter fitting and demonstrates that the behavior of nanoparticles can be systematically understood in terms of the dimensionless scaling.

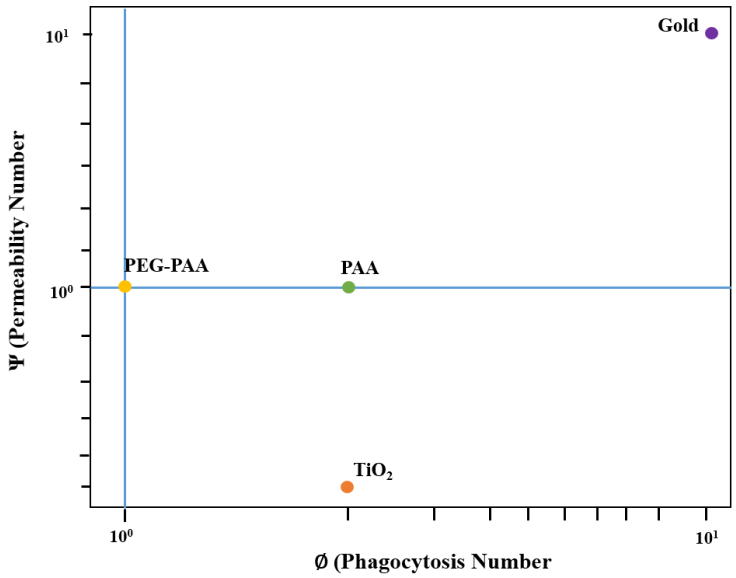


Figure 5: Ø – Ψ Regime with Nanoparticles

5.5 Effect of Ø on Accumulation

The impact of phagocytosis (Ø) on the kinetics of nanoparticle accumulation is shown in Figure 6. The mechanism shifts from perfusion-controlled transport to phagocytosis-dominated sequestration as Ø increases, leading to a broader and quicker accumulation.

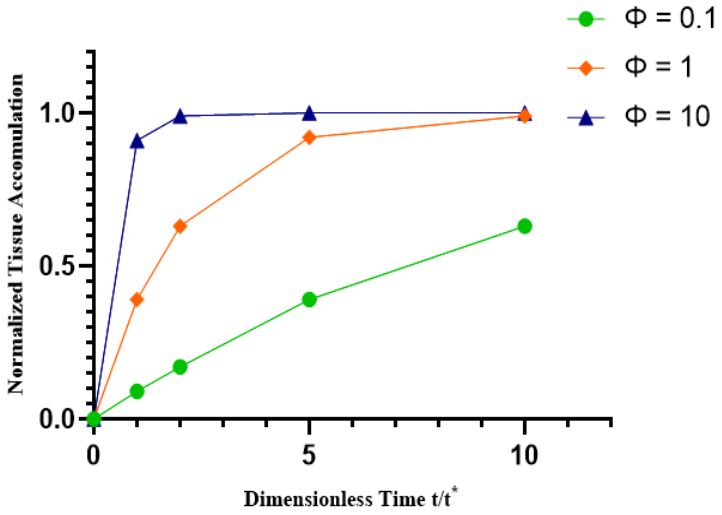


Figure 6: Effect of Ø on Accumulation

6. Discussion

Despite variations in composition (PAA-PEG, PAA, gold, and TiO_2), dose, and size, our PBPK model, a further development of a model first optimized for PAA-PEG NPs accurately describes the biokinetic profiles of four distinct types of NPs, as demonstrated by strong correlations between the simulated and observed amounts in the majority of the organs

and tissues examined. This implies that the biokinetics of other intravenously administered non-degradable NPs may also be explained by model. The grouping of free parameters in Figure 2 effectively describes the dynamics of TiO_2 NP concentrations in different tissues without overfitting, demonstrating the predictive potential of the parsimonious model. Additionally, Figure 4 demonstrates the local sensitivity of liver and spleen exposures to ±10% changes in the important parameters. Spleen exposures are sensitive to cellular uptake rate (k_{ab0}), whereas liver AUC is more susceptible to changes in extracellular space factors like solute radius and vascular permeability. The acknowledged differences in these two organs' capacity to phagocytose are the cause of this discrepancy (Owens III & Peppas, 2006; Sarin, 2010).

The mathematical reasoning for how nanoparticles travel through the body is shown in this study, which goes beyond the majority of PBPK research that only modify parameters. The researchers identify universal patterns in nanoparticle movement by introducing dimensionless groups such as Φ and Ψ. Numerous experimental studies have demonstrated that these biokinetics are strongly reliant on the characteristics of the NPs, as seen by the substantial discrepancies in several parameters (Khlebtsov & Dykman, 2011; Lin et al., 2015; Owens III & Peppas, 2006).

The location of several nanoparticles in this phase space demonstrates that phagocytic uptake (ø) and vascular permeability (Ψ) interact to determine biodistribution, not the values of individual parameters. Similar conceptual frameworks have been put forth in PBPK modeling studies where prominent physiological processes such cellular uptake saturation, permeability restriction, and perfusion limitation result in transport regimes. For instance, rather of using case-specific fitting, Carlander et al. (2016) have demonstrated that the biodistribution of nanoparticles may be generalized based on physiologically appropriate parameter groups. According to Yuan et al. (2019) regime-based interpretations also enhance the prediction power of NP-PBPK systems (Shi et al., 2018).

The absorption of NPs by PCs and the subsequent saturation of these cells is a crucial component of our concept. PCs, particularly those found in the organs of the mononuclear phagocyte system, such as the liver, spleen, and bone marrow, absorb NPs delivered into the circulation (Owens III & Peppas, 2006; Saba, 1970; Sarin, 2010). Furthermore, large intravenous NP dosages have been shown to overload the liver and alter biokinetics. PAA-PEG and PAA NPs show that NPs are absorbed by other organs, including kidneys, bone marrow, and lungs, when the liver becomes saturated (Panagi et al., 2001).

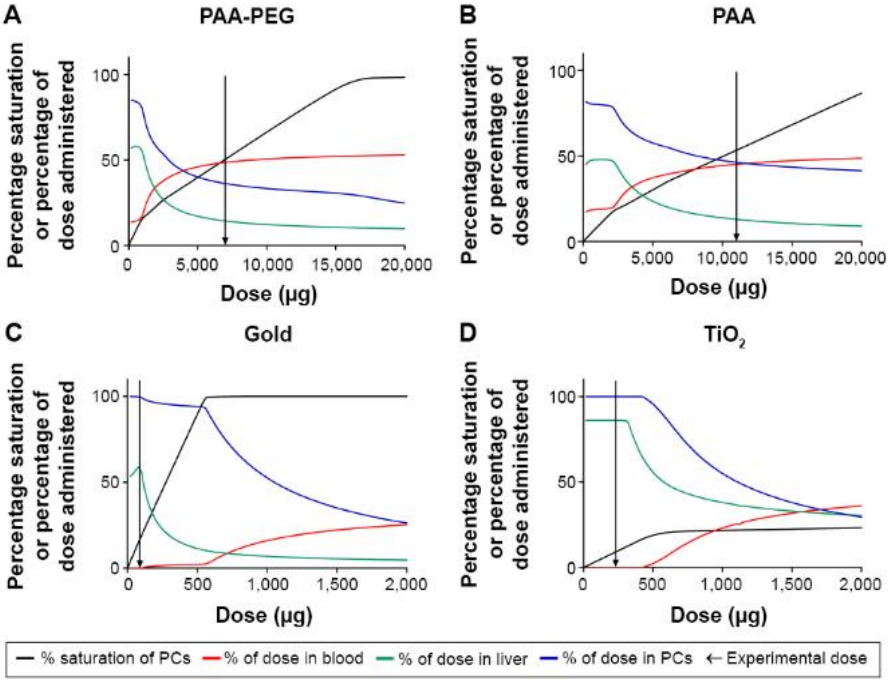


Figure 7: By this Model, the Biokinetics of the Four Kinds of Nanoparticles at Various Dosages were Estimated

Notes: Rats were Given Intravenous Injections of (A) PEGylated polyacrylamide (PAA-PEG), (B) Uncoated Polyacrylamide (PAA), (C) Gold and (D) Titanium Dioxide (TiO_2) Nanoparticles 24 Hours Later. The Estimation Curves Show the Percentage of the Dose Recovered in Liver, blood, and Phagocytic Cells (PCs) as well as the Percentage Saturation of PCs at Various Doses. The Dosages used by Wenger et al. (2011), Wang et al. (2010), and Shinohara et al. (2014) are Shown by the Vertical Arrows.

Increasing the phagocytosis number (ø) causes the nanoparticle kinetics to change from perfusion-controlled

distribution to phagocytosis-dominated sequestration, as seen in Figure 6. This results in a higher and faster accumulation in organs with high activity of the mononuclear phagocyte system (MPS). The rate of nanoparticle accumulation in the liver and spleen is significantly increased by opsonization-mediated phagocytosis, according to Owens III and Peppas (2006). Similarly, Lin et al. (2022) showed that biodistribution patterns were significantly impacted by nonlinear uptake kinetics brought on by macrophage saturation.

7. Conclusion

This work provides a generic biomathematical method that uses an expanded physiological-based pharmacokinetic (PBPK) model with dimensionless analysis and parameter reduction to characterize the biodistribution of nanoparticles. This model moves beyond parameter fitting to a theoretical foundation of transport behavior with the addition of the phagocytosis number (∅) and the permeability number (Ψ). These non-dimensional numbers offer a way to differentiate between various biodistribution regimes and explain the fundamental governing principles of nanoparticle dynamics. By reducing structural complexity without sacrificing predictive ability, this technique is able to reliably forecast the biokinetics of different nanoparticles-based biomaterials despite variations in physicochemical properties. The ∅ – Ψ method is particularly helpful as a scalable and predictive paradigm for explaining how differences in phagocytosis and permeability affect organ distribution. All things considered, this work creates a mathematical method for modeling NP-PBPK systems that improves interpretability, gets rid of unnecessary factors, and offers more predictive insights. The model provides a foundation for future advancements and enhancements in this area, such as the creation and refinement of nano-drug delivery systems.

8. References

Aborig, M., Malik, P. R., Nambiar, S., Chelle, P., Darko, J., Mutsaers, A., Edginton, A. N., Fleck, A., Osei, E., & Wettig, S. (2019). Biodistribution and physiologically-based pharmacokinetic modeling of gold nanoparticles in mice with interspecies extrapolation. *Pharmaceutics*, *11*(4), 179.

Alpini, G., Phillips, J. O., Vroman, B., & Larusso, N. F. (1994). Recent advances in the isolation of liver cells. *Hepatology*, *20*(2), 494-514.

Bernareggi, A., & Rowland, M. (1991). Physiologic modeling of cyclosporin kinetics in rat and man. *Journal of pharmacokinetics and biopharmaceutics*, *19*(1), 21-50.

Brown, R. P., Delp, M. D., Lindstedt, S. L., Rhomberg, L. R., & Beliles, R. P. (1997). Physiological parameter values for physiologically based pharmacokinetic models. *Toxicology and industrial health*, *13*(4), 407-484.

Carlander, U., Li, D., Jolliet, O., Emond, C., & Johanson, G. (2016). Toward a general physiologically-based pharmacokinetic model for intravenously injected nanoparticles. *International journal of nanomedicine*, 625-640.

Cho, T., Hayes, A., Henderson, J. T., & Uetrecht, J. (2024). The use of PD-1 functional knockout rats to study idiosyncratic adverse reactions to nevirapine. *Toxicological Sciences*, *200*(2), 382-393.

Dadashova, K., Smith, R. C., & Haider, M. A. (2024). Local identifiability analysis, parameter subset selection and verification for a minimal brain PBPK model. *Bulletin of Mathematical Biology*, *86*(2).

Eriksson, E., Royo, F., Lyberg, K., Carlsson, H. E., & Hau, J. (2004). Effect of metabolic cage housing on immunoglobulin A and corticosterone excretion in faeces and urine of young male rats. *Experimental physiology*, *89*(4), 427-433.

Fjóla, J. (2025). Editorial for the Special Issue “Mathematical Modelling in Drug Delivery”. *Pharmaceutics*, *17*(7), 871.

Frigell, J., García, I., Gómez-Vallejo, V., Llop, J., & Penades, S. (2014). 68Ga-labeled gold glyconanoparticles for exploring blood–brain barrier permeability: preparation, biodistribution studies, and improved brain uptake via neuropeptide conjugation. *Journal of the American Chemical Society*, *136*(1), 449-457.

Geraets, L., Oomen, A. G., Krystek, P., Jacobsen, N. R., Wallin, H., Laurentie, M., Verharen, H. W., Brandon, E. F., & de Jong, W. H. (2014). Tissue distribution and elimination after oral and intravenous administration of different titanium dioxide nanoparticles in rats. *Particle and fibre toxicology*, *11*(1), 30.

Hsieh, N.-H., Reisfeld, B., Bois, F. Y., & Chiu, W. A. (2018). Applying a global sensitivity analysis workflow to improve the computational efficiencies in physiologically-based pharmacokinetic modeling. *Frontiers in pharmacology*, *9*, 588.

Jain, K., Verma, A. K., Mishra, P. R., & Jain, N. K. (2015). Characterization and evaluation of amphotericin B loaded MDP conjugated poly (propylene imine) dendrimers. *Nanomedicine: Nanotechnology, Biology and Medicine*, *11*(3), 705-713.

Jones, H., & Rowland-Yeo, K. (2013). Basic concepts in physiologically based pharmacokinetic modeling in drug discovery and development. *CPT: pharmacometrics & systems pharmacology*, *2*(8), 1-12.

Karlsson, F. H., Bouchene, S., Hilgendorf, C., Dolgos, H., & Peters, S. A. (2013). Utility of in vitro systems and preclinical data for the prediction of human intestinal first-pass metabolism during drug discovery and preclinical development. *Drug Metabolism and Disposition*, *41*(12), 2033-2046.

Khlebtsov, N., & Dykman, L. (2011). Biodistribution and toxicity of engineered gold nanoparticles: a review of in vitro and in vivo studies. *Chemical Society Reviews*, *40*(3), 1647-1671.

Kolhar, P., Anselmo, A. C., Gupta, V., Pant, K., Prabhakarpandian, B., Ruoslahti, E., & Mitragotri, S. (2013). Using shape effects to target antibody-coated nanoparticles to lung and brain endothelium. *Proceedings of the National Academy of Sciences*, *110*(26), 10753-10758.

Krishnan, K., Haddad, S., & Pelekis, M. (1995). A simple index for representing the discrepancy between simulations of physiological pharmacokinetic models and experimental data. *Toxicology and industrial health*, *11*(4), 413-421.

Le, A. D., Wearing, H. J., & Li, D. (2022). Streamlining physiologically-based pharmacokinetic model design for intravenous delivery of nanoparticle drugs. *CPT: pharmacometrics & systems pharmacology*, *11*(4), 409-424.

Li, D., Johanson, G., Emond, C., Carlander, U., Philbert, M., & Jolliet, O. (2014). Physiologically based pharmacokinetic modeling of polyethylene glycol-coated polyacrylamide nanoparticles in rats. *Nanotoxicology*, *8*(sup1), 128-137.

Lin, Z., Monteiro-Riviere, N. A., & Riviere, J. E. (2015). Pharmacokinetics of metallic nanoparticles. *Wiley Interdisciplinary Reviews: Nanomedicine and Nanobiotechnology*, *7*(2), 189-217.

Lin, Z. P., Nguyen, L. N., Ouyang, B., MacMillan, P., Ngai, J., Kingston, B. R., Mladjenovic, S. M., & Chan, W. C. (2022). Macrophages actively transport nanoparticles in tumors after extravasation. *ACS nano*, *16*(4), 6080-6092.

Onofri, E., Cristiani, E., Martelli, A., Gentile, P., Hernández, J. G., & Pontrelli, G. (2025). A general multi-stratum model for a nanofunctionalized releasing capsule: a computational study. *arXiv preprint arXiv:2506.17078*.

Owens III, D. E., & Peppas, N. A. (2006). Opsonization, biodistribution, and pharmacokinetics of polymeric nanoparticles. *International journal of pharmaceutics*, *307*(1), 93-102.

Ozbek, O., Genc, D. E., & O. Ulgen, K. (2024). Advances in physiologically based pharmacokinetic (PBPK) modeling of nanomaterials. *ACS Pharmacology & Translational Science*, *7*(8), 2251-2279.

Panagi, Z., Beletsi, A., Evangelatos, G., Livaniou, E., Ithakissios, D., & Avgoustakis, K. (2001). Effect of dose on the biodistribution and pharmacokinetics of PLGA and PLGA–mPEG nanoparticles. *International journal of pharmaceutics*, *221*(1-2), 143-152.

Saba, T. M. (1970). Physiology and physiopathology of the reticuloendothelial system. *Archives of internal medicine*, *126*(6), 1031-1052.

Sarin, H. (2010). Physiologic upper limits of pore size of different blood capillary types and another perspective on the dual pore theory of microvascular permeability. *Journal of angiogenesis research*, *2*(1), 14.

Shi, Y., Jiang, Y., Cao, J., Yang, W., Zhang, J., Meng, F., & Zhong, Z. (2018). Boosting RNAi therapy for orthotopic glioblastoma with nontoxic brain-targeting chimaeric polymersomes. *Journal of controlled release*, *292*, 163-171.

Shinohara, N., Danno, N., Ichinose, T., Sasaki, T., Fukui, H., Honda, K., & Gamo, M. (2014). Tissue distribution and clearance of intravenously administered titanium dioxide (TiO2) nanoparticles. *Nanotoxicology*, *8*(2), 132-141.

Sonavane, G., Tomoda, K., & Makino, K. (2008). Biodistribution of colloidal gold nanoparticles after intravenous administration: effect of particle size. *Colloids and Surfaces B: Biointerfaces*, *66*(2), 274-280.

Travlos, G. S. (2006). Normal structure, function, and histology of the bone marrow. *Toxicologic pathology*, *34*(5), 548-565.

Wang, J., Xie, X., Cao, X., & Sun, L. (2025). Prediction of in vivo behavior of nanoparticles using physiologically based pharmacokinetic Model: The modeling approach and issues. *European Journal of Pharmaceutics and*

Biopharmaceutics, 114943.

Wang, L., Li, Y.-F., Zhou, L., Liu, Y., Meng, L., Zhang, K., Wu, X., Zhang, L., Li, B., & Chen, C. (2010). Characterization of gold nanorods in vivo by integrated analytical techniques: their uptake, retention, and chemical forms. *Analytical and bioanalytical chemistry*, *396*(3), 1105-1114.

Wenger, Y., Schneider II, R. J., Reddy, G. R., Kopelman, R., Jolliet, O., & Philbert, M. A. (2011). Tissue distribution and pharmacokinetics of stable polyacrylamide nanoparticles following intravenous injection in the rat. *Toxicology and applied pharmacology*, *251*(3), 181-190.

Wu, J., Wick, P., & Nowack, B. (2025). Data-driven prediction of nanoparticle biodistribution from physicochemical descriptors. *ACS nano*, *19*(29), 26425-26437.

Yokel, R., Grulke, E., & MacPhail, R. (2013). Metal-based nanoparticle interactions with the nervous system: the challenge of brain entry and the risk of retention in the organism. *Wiley Interdisciplinary Reviews: Nanomedicine and Nanobiotechnology*, *5*(4), 346-373.

Yuan, D., He, H., Wu, Y., Fan, J., & Cao, Y. (2019). Physiologically based pharmacokinetic modeling of nanoparticles. *Journal of pharmaceutical sciences*, *108*(1), 58-72.